



ELSEVIER

Available online at [www.sciencedirect.com](http://www.sciencedirect.com)

SCIENCE @ DIRECT®

Optics Communications 218 (2003) 173–182

OPTICS  
COMMUNICATIONS

[www.elsevier.com/locate/optcom](http://www.elsevier.com/locate/optcom)

# Temperature dependent determination of the linear electrooptic coefficient $r_{33}$ in $\text{Sr}_{0.61}\text{Ba}_{0.39}\text{Nb}_2\text{O}_6$ single crystals by means of light-induced scattering

M. Goulkov<sup>a,\*</sup>, T. Granzow<sup>b</sup>, U. Dörfler<sup>b</sup>, Th. Woike<sup>b</sup>, M. Imlau<sup>c</sup>, R. Pankrath<sup>c</sup>,  
W. Kleemann<sup>d</sup>

<sup>a</sup> *Institute of Physics, Science Ave 46, 03650 Kiev-39, Ukraine*

<sup>b</sup> *Institute for Mineralogy and Geochemistry, University of Cologne, Zùlpicherstr. 49b, D-50674 Cologne, Germany*

<sup>c</sup> *Department of Physics, University Osnabrück, Barbarastr. 7, D-49069 Osnabrück, Germany*

<sup>d</sup> *Laboratory for Applied Physics, Gerhard-Mercator-University Duisburg, Lotharstr. 65, D-47048 Duisburg, Germany*

Received 17 June 2002; received in revised form 1 August 2002; accepted 30 January 2003

## Abstract

The temperature dependence of the light-induced polarization–isotropic scattering in strontium–barium–niobate (SBN) doped with 0.66 mol% cerium is studied in a temperature range covering the ferroelectric phase and the relaxor phase transition. We introduce a method to determine the electrooptic coefficient  $r_{33}$  and the effective density of the photorefractive centers  $N_{\text{eff}}$  from the angular distribution of the scattered light. The temperature dependence of these two parameters is discussed with respect to the phase-transition behavior.

© 2003 Elsevier Science B.V. All rights reserved.

PACS: 42.65.Hw; 7.80.-e; 78.20.Jq

## 1. Introduction

Strontium–barium–niobate ( $\text{Sr}_x\text{Ba}_{1-x}\text{Nb}_2\text{O}_6$ , SBN) has received much attention with regard to both scientific studies of its electrooptic properties [1] and possible applications in the field of electrooptic materials such as holographic storage [2,3] or phase-conjugated mirrors [4]. This interest

has been fueled by the large electrooptic effect exhibited by SBN [1,5] and the possibility to grow crystals of the congruently melting composition with  $x = 0.61$  (SBN61) with very good optical quality [6]. The electrooptic properties of SBN61 can be further improved by doping. Ce-doping, for example, leads to a significant increase of the linear electrooptic coefficients and the sensitivity of the crystal to light of larger wavelengths [7], extending the wavelength range that is available for photorefractive applications from the low ultraviolet to the near infrared spectral range. Doping also lowers the temperature of the phase transition

\* Corresponding author. Tel.: +38-44-265-0818; fax: +38-44-265-2359.

E-mail address: [goulkov@iop.kiev.ua](mailto:goulkov@iop.kiev.ua) (M. Goulkov).

from the ferroelectric low-temperature phase into the centrosymmetric, paraelectric high-temperature phase from about 80 °C for the undoped sample down to room temperature for crystals doped with 2.07 mol% cerium. The relatively low coercive field of a few hundred (V/mm) [8,9] allows an easy adjustment of the ferroelectric domain structure, resulting in special domain configurations such as in periodically poled crystals [10,11]. All these properties make SBN an ideal candidate for the examination and application of electrooptic and nonlinear optic effects.

In the context of domain configurations, the question of the phase-transition behavior of SBN is also of interest. The phase transition from the ferroelectric into the paraelectric phase does not happen at a well-defined critical transition temperature, as theory predicts for ferroelectrics, but it is ‘smeared’ over a wide temperature range [12,13]. Due to this relaxor phase transition, phenomena that are typical for noncentrosymmetric materials, such as the electrooptic effect, occur even in a temperature range that can already be considered as the paraelectric, centrosymmetric high-temperature phase [14].

Since the linear electrooptic effect is a major factor behind most nonlinear optic phenomena in ferroelectric crystals (including photorefraction), intimate knowledge of electrooptic properties is important not only for many technological applications [15,16] but also for a clear understanding of nonlinear optical processes in these crystals. In the case of SBN (point symmetry group 4 mm), the third rank electrooptic tensor  $\hat{r}$  has only three independent components:  $r_{33}$ ,  $r_{13}$  and  $r_{42}$ . However, the procedure of a precise experimental determination of the electrooptic coefficients is not trivial and still poses very high technological demands. Normally, these coefficients are measured by interferometric methods which require a very high mechanical stability as well as a high temperature stability of the measurement equipment [5,17]. Furthermore, this method requires an external electric ac field to be applied to the sample, a process which can influence the ferroelectric polarization and thus the electrooptic behavior. As an alternative, measurements of the angular dependence of the holographic two-beam coupling

gain  $\Gamma$  by a holographic two-beam coupling method have been proposed to determine all three components of the electrooptic tensor in SBN [18]. This method eliminates the need for external electric fields. However the internal electric field induced in the bulk of the crystal by coherent illumination amounts to about 100 V/mm and may influence the measurement of the electrooptic coefficients. The requirements to mechanical stability also remain and are similar to the interferometric technique. It is therefore desirable to develop a method of measuring the electrooptic coefficients that combines the field-free technique of holography with low experimental demands. The effect of light-induced scattering proves to be a valuable tool that has both of these advantages. Light-induced scattering accompanies the propagation of a laser beam in a photorefractive crystal and often draws a significant part of the beam intensity. In the case of a SBN crystal, the strongest scattering is polarization–isotropic wide-angle scattering appearing from an extraordinarily polarized pump beam. In the literature this is also referred to as photoinduced scattering [19], beam fanning [23], asymmetric light induced stimulated scattering [24] or holographic light scattering [14]. It originates from primary scattering of the incident beam on optical imperfections in the crystal volume. This coherent optical seed light interferes with the transmitted light and records a multitude of parasitic photorefractive gratings. Due to the nonlinear coupling of seed and pump waves on the parasitic gratings, a part of the primary scattering can be amplified at the expense of the pump beam, resulting in light-induced scattering. It has been shown that the well-known theory of two-beam coupling in the case of a small signal beam amplification can be applied in the description of the final scattering pattern [19,20]. Since the beam-fanning has a considerably wide angular indicatrix and the total scattering intensity is distributed over large space angles, the internal electric fields induced in SBN do not exceed a few V/cm, and that can not significantly influence the measurement of the value of the electrooptic coefficients in the crystal. The study of the beam fanning does not require high mechanical stability for the experimental setup.

In this paper we show that the examination of the light-induced scattering in highly doped SBN61:Ce is an easy way to determine the angular dependence of the holographic two-beam coupling gain  $\Gamma$  from only one measurement. The resulting  $\Gamma(\theta)$ -distribution is used to obtain both the electrooptic coefficient  $r_{33}$  and the effective trap density  $N_{\text{eff}}$  of a Ce-doped SBN61 single crystal. The temperature dependence of these parameters is examined in a temperature range encompassing the ferroelectric low-temperature phase, the relaxor regime and the paraelectric high-temperature phase where the light-induced scattering finally vanishes. The results are discussed with respect to the relaxor nature of the phase transition.

## 2. Experimental setup

A single crystal of SBN61 doped with 0.66 mol% cerium was grown by the Czochralski technique and cut parallel to the crystallographic axes into a rectangular parallelepiped with dimensions of  $0.90 \times 7.15 \times 6.20 \text{ mm}^3$  along the  $a$ -,  $b$ - and  $c$ -axis, respectively. The temperature of the phase transition between the paraelectric and the ferroelectric state is found at  $T = 52 \text{ }^\circ\text{C}$  [25]. The sample was poled by heating up to  $140 \text{ }^\circ\text{C}$ , applying an external electric field of  $350 \text{ V/mm}$  along the crystallographic  $c$ -axis and then slowly cooling down to room temperature before removing the field. This procedure results in a sample where practically all existing domains are aligned according to the external field [26]. Then the sample was placed in a holder and fixed on a thermoelectric element. A temperature controller allowed to adjust the sample temperature from  $10$  to  $150 \text{ }^\circ\text{C}$  with an absolute accuracy of  $0.3 \text{ }^\circ\text{C}$ . The faces of the sample normal to the crystallographic  $c$ -axis were short circuited to prevent an influence of pyroelectric fields when the sample temperature was changed.

A sketch of the setup can be seen in Fig. 1. The beam of a low-power He–Ne-laser serving as the pump beam with a wavelength of  $\lambda = 632.8 \text{ nm}$  was directed normally on the large  $a$ -face of the sample. The polarization of the beam was oriented parallel to the  $c$ -axis of the sample. The intensity of

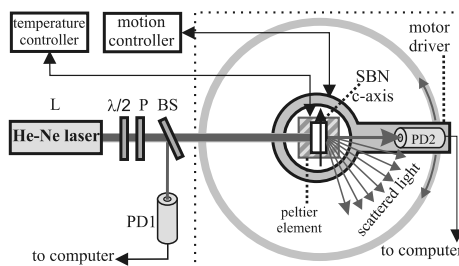


Fig. 1. (a) Experimental setup for measuring the angular distribution of the scattered light at different temperatures. L is a He–Ne-laser,  $\lambda/2$  a half-wave retarder plate, P a Glan–Thomson prism, BS a beam splitter, PD1 and PD2 are photodiodes. The SBN61:Ce (0.66 mol%) sample is placed on a stack of Peltier-elements to regulate the temperature.

the pump beam was adjusted to a value of  $70 \text{ mW/cm}^2$  using a half-wave retarder plate and a Glan–Thomson prism. This low intensity was chosen to prevent nonlinear effects other than light-induced scattering that might influence our measurement. The pump beam had a Gaussian intensity distribution with a FWHM of  $0.8 \text{ mm}$ . A small fraction of the pump beam was directed to a photodiode PD1 by a beamsplitter BS to monitor the laser intensity. Photodiode PD2 was placed behind the sample at a distance of  $5.5 \text{ cm}$  and was mounted on a rotation stage driven by an electronic motion controller. When moving, photodiode PD2 made an exact half-circle around the sample in the direction from the negative to the positive end of the polarization vector in order to measure the light distribution in the plane of incidence parallel to the  $c$ -axis. The scattered light is measured in the angular range  $-90^\circ \leq \theta_s \leq +90^\circ$ , where the negative and positive scattering angles  $\theta_s$  correspond to the scattering against and along the direction of the polar  $c$ -axis, respectively. At  $\theta_s = 0^\circ$  the photodiode crosses the pump beam directly behind the crystal. The aperture of the diaphragm on PD2 limits the apex angle of the measured scattered light to  $0.5^\circ$ . The entire setup is enclosed in a black box (represented by the dotted rectangle in the figure) with only a small opening for the pump beam to minimize the noise due to external light sources. To obtain a baseline curve, the intensity distribution of the laser was measured without a sample in the holder.

### 3. Experimental results

Immediately after the beginning of the illumination, very weak scattering with an isotropic angular distribution appears around the transmitted laser beam. This initial scattering pattern then develops into the well-known asymmetric scattering pattern [14] where the light is strongly enhanced in the direction antiparallel to the polar  $c$ -axis of the crystal. Correspondingly, the scattered intensity is depleted in the direction parallel to the  $c$ -axis. The intensity of the transmitted pump beam decreased by about 60% during this process. After about 15 min, the temporal development of the scattering pattern reaches a steady state. An angular scan over the intensity distribution of the scattered light at  $T = 20^\circ\text{C}$  is presented in Fig. 2. The values have been normalized to the maximum of the transmitted intensity and plotted on a logarithmic scale to allow a better comparison. The angular asymmetry is clearly noticeable: On the left-hand side, at negative angles, there is a large scattering intensity with a broad maximum at  $\theta_s = -28^\circ$ . At  $\theta_s = 0^\circ$ , the diode crosses the transmitted pump beam, more than five orders of magnitude larger than the scattered intensity. On the right-hand side, at positive scattering angles, the intensity of the scattered light is two orders of magnitude smaller than the one at negative scattering angles. The sharp peak at  $\theta_s = -80^\circ$  is due to internal reflections at the inner crystal faces. When the sample is heated, the scattering pattern changes: The total scattered intensity increases, the maximum in the negative direction becomes more

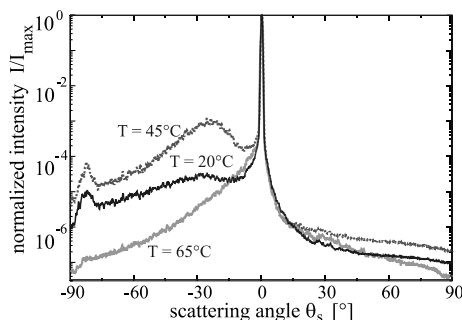


Fig. 2. Angular distribution of the scattered light in SBN in the ferroelectric state ( $T = 20^\circ\text{C}$ ), in the transition range ( $T = 45^\circ\text{C}$ ) and the relaxor state ( $T = 65^\circ\text{C}$ ).

pronounced and shifts closer to the transmitted pump line at  $0^\circ$ . As an example, the scattering pattern measured at  $T = 45^\circ\text{C}$  is also presented in Fig. 2. When the phase transition temperature is exceeded at  $T = 52^\circ\text{C}$ , the light-induced scattering does not vanish abruptly, as it would in ferroelectrics with a critical phase transition. Instead, an asymmetric scattering pattern is still observed for higher temperatures, with a decrease of the total scattered intensity and a further shift of the maximum towards smaller scattering angles. This behavior is exemplarily shown in Fig. 2 for the scattering pattern observed at  $T = 65^\circ\text{C}$ . At a temperature of  $T = 100^\circ\text{C}$ , the light-induced scattering pattern finally vanishes into the background noise.

### 4. Discussion

The observed angular dependence of the scattered intensity at different temperatures corresponds very well with the results reported previously [25]. As it is shown in [19,20], the wide-angle polarization–isotropic scattering (beam fanning) arising in SBN during illumination of the crystal by a single laser beam is a typical photorefractive phenomenon. It results from nonlinear amplification of the scattered part of the incident beam at the expense of the transmitted part, when the scattered and transmitted light records noisy gratings of the refractive index and interacts on them. In order to simplify the model equations and the numerical treatment of the experimental results, below an unsophisticated microscopic photorefractive model [21] is applied to analyze the spatial distribution of the beam fanning in SBN:Ce. We restrict ourselves by the following assumptions: (i) diffusion of photocarriers is the dominating charge transport mechanism in SBN in the absence of an external electric field, and the contribution of a photovoltaic effect is negligibly small [22]; (ii) electrons are major contributors to the photoinduced current [27], and deep centers associated with  $\text{Ce}^{3+}$  ions donate photoelectrons, whereas  $\text{Ce}^{4+}$  ions serve as deep trapping centers. Minor contribution of positive charges (holes) in the diffusion transport is possible in SBN, and it

can slightly modify the resulting space-charge field; (iii) contributions of shallow traps in the formation of the space charge field  $E_{sc}$  and the contribution of dark conductivity to the total crystal conductivity are neglected; (iv) an undepleted pump approximation is used in the case of the light-induced scattering; (v) the absorption coefficient  $\alpha$  can be approximated to zero, which is quite realistic for SBN:Ce illuminated at  $\lambda = 633$  nm.

According to [19], the incident pump beam scatters on surface imperfections and on optical inhomogeneities in the crystal volume. Coherent waves of the initial scattering serve as a seed for the beam fanning. A pair of transmitted (pump) and scattered (seed) light waves forms an elementary light intensity pattern  $I(\mathbf{r}) = (I_s + I_p)(1 + m \cos(\mathbf{K} \cdot \mathbf{r}))$  with the modulation depth  $m = 2\sqrt{I_s I_p}/(I_s + I_p)$ . The interference pattern consists of bright and dark fringes periodically sequenced along the grating vector  $K_g$  with absolute value

$$K_g = 2\pi/\Lambda = 4\pi \sin \theta_s^{\text{in}}/\lambda, \quad (1)$$

where  $\theta_s^{\text{in}}$  is the scattering angle between seed and pump waves inside the crystal.

The spatially inhomogeneous elementary light pattern excites electrons from donors into the conduction band. Due to the diffusion process, photocarriers are migrating from bright fringes to dark fringes and are trapped there by acceptors. The resulting electric space charge field is shifted in space by  $\Lambda/4$  with respect to the original interference light pattern:  $E_{sc}(\mathbf{r}) = mE_{sc}^0 \sin(K_g \cdot \mathbf{r})$ . The amplitude  $E_{sc}^0$  of this space charge field can be written as [28]

$$E_{sc}^0 = \zeta \frac{k_B T}{e} \frac{K_g}{1 + (K_g/K_d)^2} (\mathbf{e}_p \cdot \mathbf{e}_s) \quad (2)$$

where  $k_B$  is Boltzmann's constant,  $T$  is the temperature,  $e$  is the unit charge,  $\mathbf{e}_p$  and  $\mathbf{e}_s$  are the polarization unit vectors of pump and scattered wave, respectively. Coefficient  $\zeta \leq 1$  is introduced to account for the electron-hole competition, when that occurs. If electrons are major photocarriers in the crystal, then  $\zeta \approx 1$ . The parameter

$$K_d = \sqrt{\frac{e^2 N_{\text{eff}}}{\epsilon_{33} \epsilon_0 k_B T}}$$

takes into account the effect of the Debye screening that reduces the amplitude of the space charge field in SBN at large spatial frequencies.  $N_{\text{eff}} = (c_{\text{Ce}^{3+}} \cdot c_{\text{Ce}^{4+}})/(c_{\text{Ce}^{3+}} + c_{\text{Ce}^{4+}})$  is the effective trap density, where  $c_{\text{Ce}^{3+}}$  and  $c_{\text{Ce}^{4+}}$  are the volume concentrations of Ce in the corresponding charge states, and can be approximated by  $N_{\text{eff}} \approx c_{\text{Ce}^{4+}}$ , since  $c_{\text{Ce}^{3+}} \gg c_{\text{Ce}^{4+}}$  [30].  $(\mathbf{e}_p \cdot \mathbf{e}_s) \approx 1$  in our case.

The main disadvantage of the microscopic approach to photorefractive phenomena is that this description deals with microscopic properties of the ferroelectric crystal, and these properties differ from one sample to another and are almost non-controllable. Even in the case of the simplest one-species–one-carrier model, the expression for the space charge field  $E_{sc}^0$  contains at least one free parameter, namely  $N_{\text{eff}}$ . There is also an alternative macroscopic approach to the description of photorefractive phenomena [31], where the functional relations for  $E_{sc}$  are phenomenologically established according to the crystal symmetry. The phenomenological description applies more general statements than the microscopic approach and uses only macroscopic parameters. Those can be directly measured in the experiment. However, when applied to SBN, the macroscopic description has serious limitations at high spatial frequencies and therefore is not able to account for the Debye screening important for the spatial separation of photoinduced charges at  $\Lambda \ll K_d^{-1}$ . At the same time, the microscopic model adequately describes the photorefractive response both at high and low spatial frequencies.

Since there is always a multitude of scattered light waves in all directions in the crystal, the resulting space charge field consists of a rather complicated superposition of elementary electric space charge fields. In an electrooptic crystal, a single electric charge grating causes a spatial modulation of the refractive index  $\Delta n(\mathbf{r})$  that follows the profile of the space-charge field:  $\Delta n(\mathbf{r}) = \Delta n_o \sin(K_g \cdot \mathbf{r})$ . The amplitude of the resulting refractive index grating is proportional to the amplitude of the corresponding space charge field:

$$\Delta n_o = -\frac{1}{2} n_{\text{eff}}^3 r_{\text{eff}} E_{sc}, \quad (3)$$

where  $n_{\text{eff}}$  and  $r_{\text{eff}}$  are the effective values of the refractive index and the linear electrooptic coefficient,

cient. Hence the electrooptic effect exhibits a strong anisotropy, and index gratings can be recorded only when the corresponding component of the electrooptic tensor is not equal to zero. In the case of SBN, this is true only for  $r_{33}$ ,  $r_{13}$  and  $r_{42}$ . Extraordinarily polarized pump and seed waves record only gratings with grating vectors which have nonzero projections  $K_g^z$  along the  $c$ -axis. The larger  $K_g^z$  is, the stronger the corresponding phase grating becomes.

The spontaneous polarization  $P_s$  in SBN is attributed to the displacement of metal atoms from the oxygen planes along the fourfold axis of the  $\text{NbO}_6$  octahedra [32] when the crystal undergoes the phase transition from the centrosymmetric into the noncentrosymmetric phase. The field of the spontaneous polarization causes further distortion of the elementary crystal lattice. In turn, the distortion of the centrosymmetrical crystal lattice leads to an appearance of the linear electrooptic effect. The relation between the electrooptic coefficient and the spontaneous polarization is [33,34]

$$r_{\text{eff}} \approx \cos^2 \theta r_{33} = 2 \cos^2 \theta \epsilon_0 \epsilon_{33} g_{33} P_s, \quad (4)$$

where  $g_{33}$  is the quadratic electrooptic coefficient. Here we take into account that scattering angles  $\theta_s^{\text{in}}$  cover a small range  $-25^\circ \leq \theta_s^{\text{in}} \leq +25^\circ$ , so that the contributions of  $r_{42}$  and  $r_{13}$  can be neglected. The value of the effective refractive index in Eq. (3) is  $n_{\text{eff}} \approx n_e$ .

Only in successfully poled ferroelectrics where most of the polar domains are oriented in one direction,  $P_s$  and  $r_{\text{eff}}$  have homogeneous values across the whole sample. In unpoled ferroelectrics, different domains are not mutually aligned, and the local value and direction of  $P_s$  vary from one place to other. Therefore, the electrooptic coefficient  $r_{\text{eff}}$  is different in different nano- and micro-scale regions, and its macroscopic value can even be equal to zero. A similar situation occurs in the poled relaxor at  $T > T_c$  when the thermal energy is large enough to overcome the cooperative interaction of dipoles and only local random fields cause a correlation between elementary dipoles and yield local regions with nonzero electric polarization (polar clusters). Since in the relaxor state mutual interaction between polar microregions is suppressed, the polar clusters are randomly

oriented along the predominant axis. This also results in the varying of the local values of  $P_s$  and  $r_{\text{eff}}$  over the crystal volume and in the reduction of their macroscopic values. The value of  $r_{\text{eff}}$  decreases with increasing  $T$  until it vanishes.

The spatial  $\lambda/4$ -shift between the modulation of the refractive index and the original light intensity pattern results in an effective energy transfer between pump and seed waves interacting on the refractive index grating. Since the dominating photoexcited charge carriers are electrons and the sign of the electrooptic coefficient is positive [18,27], the energy transfer is always antiparallel to the direction of the polar  $c$ -axis: The light scattered in the  $-c$ -direction is amplified at the expense of the pump beam, light scattered in the  $+c$ -direction is depleted. These amplification-depletion processes exponentially depend on the product of the two-beam coupling coefficient  $\Gamma$  and the interaction length  $l$  of the two waves. In the steady state, the scattering component with the initial intensity  $I_s^0$  reaches a value of  $I_s = I_s^0 \exp(\Gamma l)$  at the output face of the crystal [35–37]. In the general case, the coherent seed  $I_s^0$  is formed by scattering of the incident beam on surface imperfections (surface scattering) and on optical inhomogeneities distributed in the bulk of the sample (bulk scattering). As it is shown in [38], the initial bulk scattering on optical inhomogeneities localized on domain walls is primarily responsible for the seeding of the beam fanning in SBN. Nevertheless, for the sake of simplicity and taking into account very large values of  $\Gamma$  measured in SBN, below we consider  $l$  as the thickness of the crystal measured along the direction of propagation of the pump beam (along the  $x$ -axis) and  $I_s^0$  as some effective seed intensity over the crystal. According to [38], the intensity of seed scattering  $I_s^0$  exhibits a very strong dependence on the angle  $\theta_s$ .

Assuming the undepleted pump approximation and neglecting absorption, an expression for the coupling coefficient  $\Gamma$  can be written as [29]

$$\Gamma_{\pm c} = \pm \frac{4\pi\Delta n_o}{\lambda \cos \theta_s} = \mp \frac{2\pi n_e^3 E_{\text{sc}} r_{\text{eff}}}{\lambda \cos \theta_s} \quad (5)$$

where the sign ‘ $-$ ’ applies for waves scattered in the  $+c$ -direction and the sign ‘ $+$ ’ for waves scattered in the  $-c$ -direction. The two-beam coupling experi-

ment shows that the coupling coefficient in our sample is quite large and can reach values up to  $\Gamma = 45 \text{ cm}^{-1}$  at room temperature [18].

Besides the beam-fanning nonlinearly amplified with the crystal thickness, noncoherent light scattering with an amplitude linearly dependent on  $l$  may also develop in photorefractive crystals [39]. However, if the coupling coefficient is sufficiently large (as it takes place in SBN) and the product  $\Gamma l \gg 1$ , the beam fanning will greatly exceed the linear scattering and can even entirely suppress it. Only for small values of  $\Gamma$ , the contribution of the linear scattering becomes noticeable and should not be neglected. For the sake of simplicity and taking into account our particular case of large  $\Gamma$ , we can omit the contribution of the linear scattering and consider solely the beam fanning.

Substituting the expression for the space charge field from Eqs. (2) and (4) into Eq. (5), we get

$$\Gamma(\theta_s, T) = \frac{A \sin \theta_s \cos \theta_s}{1 + B^{-2} \sin^2 \theta_s}, \quad (6)$$

$$A = \zeta r_{33} \frac{8\pi^2 n_e^3 k_B T}{e\lambda^2}, \quad (7)$$

$$B = \frac{e\lambda}{4\pi} \sqrt{\frac{N_{\text{eff}}}{\epsilon_{33}\epsilon_0 k_B T}}. \quad (8)$$

Besides the explicit temperature dependence of  $A$ , the parameters  $r_{33}$ ,  $n_e$  and  $\epsilon_{33}$  depend on the temperature, too. We also must take into account a possible temperature dependence of  $N_{\text{eff}}$ . From Eq. (6) one can see that the parameter  $A$  is a factor which influences only the amplitude of  $\Gamma(\theta_s)$  and has no effect on the angular distribution. The details of the spatial structure of the distribution, most notably the position of the maximum, are determined only by the parameter  $B$ .

We can obtain the angular distribution of the gain coefficient from the measured scattering pattern as follows: We assume that the intensity of the primary scattered light from a single scattering center is the same for both directions  $\theta_s$  and  $-\theta_s$ . It has to be noted that this assumption does not imply that the intensity distribution of the primary scattered light is homogeneous, since light scattered under different angles  $\theta_s$  will still have different intensities [38]. The values of  $\Gamma$  for two

symmetric angles  $\theta_{s1}$  and  $\theta_{s2} = -\theta_{s1}$  differ only in sign, thus taking the logarithm of the corresponding ratio of the two scattered intensities  $I_{\theta_{s1}} = I_0 \exp(+|\Gamma|_{-c}l)$  and  $I_{\theta_{s2}} = I_0 \exp(-|\Gamma|_{+c}l)$  will give us twice the absolute value of the two beam coupling gain

$$2|\Gamma|l = \ln(I_{\theta_{s1}}/I_{\theta_{s2}}) \quad (9)$$

Fig. 3 shows the calculated values of  $|\Gamma|$  versus the scattering angle  $\theta_s$  for  $T = 20 \text{ }^\circ\text{C}$  (circles),  $T = 45 \text{ }^\circ\text{C}$  (squares) and  $T = 65 \text{ }^\circ\text{C}$  (crosses). The figure shows only the coefficient  $\Gamma_{-c}$  corresponding to the  $-c$ -direction. Note that the internal scattering angle  $\theta_s^{\text{in}}$  displayed in this figure ranges from about  $-25^\circ \leq \theta_s^{\text{in}} \leq 0^\circ$ , corresponding to externally observed angles in the range of  $-90^\circ \leq \theta_s^{\text{out}} \leq 0^\circ$ , due to the large refractive index of  $n_e = 2.281$  [40].

Fits of Eq. (6) to the datapoints are represented by the continuous lines in Fig. 3, the corresponding values of the fitting parameters are  $A = 190.8 \text{ cm}^{-1}$ ,  $B = 0.2665$  for  $T = 20 \text{ }^\circ\text{C}$ ,  $A = 426.4 \text{ cm}^{-1}$ ,  $B = 0.1784$  for  $T = 45 \text{ }^\circ\text{C}$  and  $A = 445.5 \text{ cm}^{-1}$ ,  $B = 0.07942$  for  $T = 65 \text{ }^\circ\text{C}$ . The very good result of the fitting procedure performed on the  $\Gamma$ -curves is apparent and shows that the simple model considered here describes the angular distribution of the beam fanning in SBN quite successfully. At the same time, one should note that the accurate fitting of the original  $I_s$ -curves is not possible without knowledge of the angular behavior of the seed scattering  $I_s^0$ . As it is mentioned above, the initial

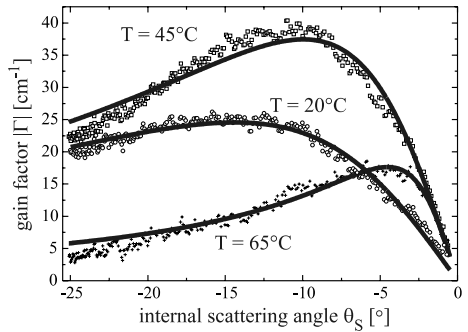


Fig. 3. Absolute value of the two beam coupling gain  $\Gamma$  versus the scattering angle  $\theta$  for  $T = 20 \text{ }^\circ\text{C}$  (circles),  $T = 45 \text{ }^\circ\text{C}$  (squares) and  $T = 65 \text{ }^\circ\text{C}$  (crosses). The solid lines are fits according to Eq. (6).

scattering exhibits a very strong dependence on the angle  $\theta_s$  [38], and this can essentially influence the real intensity distribution from sample to sample. Our method of separate extraction of  $\Gamma$ - and  $I_s^0$ -curves (Eq. (6)) allows to solve this problem. Moreover, the determination of an angular dependence of the coupling coefficient  $\Gamma$  in SBN from the scanned light-induced scattering distribution is much easier than that from the two-beam coupling experiment: we do not need to rearrange the setup to measure  $\Gamma$  for every new angle.

The variables in the parameter  $A$  besides the known temperature  $T$  are the product of the electron-hole competition factor  $\zeta$  and the electrooptic coefficient  $r_{33}$ , and the refractive index  $n_e$ . Likewise, the parameter  $B$  depends only on the quotient of the effective trap density  $N_{\text{eff}}$  and on the dielectric constant  $\epsilon_{33}$ . The material parameters  $n_e$  and  $\epsilon_{33}$  known at different temperatures allows us to determine the temperature dependence of  $\zeta r_{33}$  and  $N_{\text{eff}}$  using the proper fitting parameters  $A$  or  $B$ . Both  $\epsilon_{33}$  and  $n_e$  are known for different temperatures from [41] and [42,43], respectively. In the case of  $n_e$ , the accuracy of the published data is better than 1%, but in the case of  $\epsilon_{33}$  one has to be more careful: The published data are measured with frequencies of 100 Hz, while in our case the static dielectric constant is needed. For low temperatures, one can assume an accuracy of about 10%, but above the phase transition temperature the difference will be larger. This source of error will be discussed in detail below. Fig. 4 shows the temperature dependencies of  $\zeta r_{33}$  (upper part) and  $N_{\text{eff}}$  (lower part) calculated from the results of our fits of  $\Gamma$ -curves for all temperatures. The accuracy of the calculated values is mainly determined by the accuracy of the fitting parameters  $A$  and  $B$ . It is not possible to vary the obtained values of  $r_{33}$  and  $N_{\text{eff}}$  by more than 3% without a serious deviation of the calculated values from the experimental data, so it is safe to assume an error margin of 5% for these values. The extraction made from Fig. 4(a) for  $T = 20^\circ\text{C}$  gives  $\zeta r_{33} = (324 \pm 16)$  pm/V. In comparison, the standard interferometric method gives the value of the electrooptic coefficient also measured at  $T = 20^\circ\text{C}$  and for the same SBN sample as  $r_{33} = (354 \pm 2)$  pm/V [44]. Thus, one can deduce that the electron-hole competition

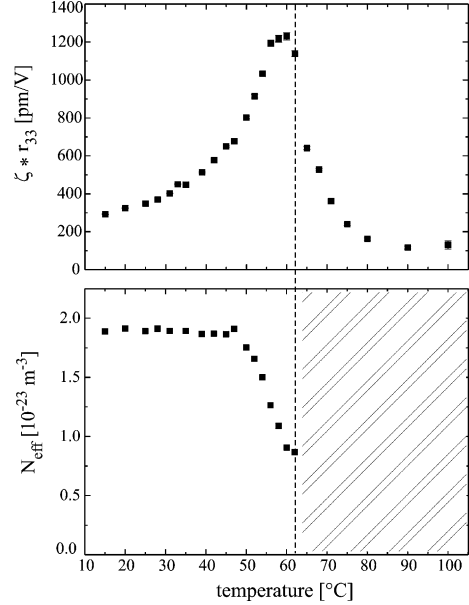


Fig. 4. Temperature dependence of the electrooptic coefficient  $r_{33}$  (top) and the effective trap density  $N_{\text{eff}}$  (bottom). Note that for  $T > 65^\circ\text{C}$   $N_{\text{eff}}$  could not be determined.

is  $\zeta \approx (0.92 \pm 0.04)$  and the product  $\zeta r_{33}$  can be substituted by only  $r_{33}$  with a quite high accuracy.

Even more so than the angular dependence of the scattered intensity itself (Fig. 2), the curves in Figs. 3 and 4 illustrate the behavior of the relevant physical parameters with increasing temperature very clearly: For low temperatures, the amplitude of  $\Gamma(\theta)$  is low, corresponding to small values of  $r_{33}$ . The maximum is very broad and lies at angles  $\theta_s^{\text{in}} \approx -15^\circ$ . The resulting values of  $r_{33}$  and  $N_{\text{eff}}$  are in good agreement with the values known from the literature [18]. When the temperature approaches the phase transition temperature, the amplitude of  $\Gamma(\theta)$  increases drastically. This is due to the strong increase in the electrooptic coefficient  $r_{33}$  near the phase transition that has already been observed in similar crystals with interferometric measurements [45]. The maximum becomes notably sharper and shifts to smaller angles due to the increase of the dielectric constant  $\epsilon_{33}$ . In contrast, the effective trap density  $N_{\text{eff}}$  remains practically constant. This is not surprising, since  $N_{\text{eff}} \approx c_{\text{Ce}^{4+}}$ . The concentration of  $\text{Ce}^{4+}$ -ions in the crystal does not change with temperature, so neither does  $N_{\text{eff}}$ .

We know that the decay of the macroscopic domain structure into smaller polar clusters starts in the temperature range between 52 °C and 65 °C [25]. In this range,  $N_{\text{eff}}$  seems to decrease significantly. However, the number of  $\text{Ce}^{4+}$ -ions in the crystal will still remain constant, and the charge transport from  $\text{Ce}^{3+}$  to  $\text{Ce}^{4+}$  will also not be so strongly affected by the slight increase of the temperature. A possible explanation of this phenomenon is an error in the determination of  $N_{\text{eff}}$  by the fitting parameter  $B$  from Eq. (6), where we used the literature values for  $\epsilon_{33}$ . These values were obtained with an ac-method at a frequency of 100 Hz, whereas in our case the static dielectric constant is needed. For temperatures below  $T_C$ , the frequency-dependence of  $\epsilon_{33}$  is not very pronounced, but in the phase transition range the formerly stable domains decay into polar clusters of different mobility. This results in a very strong dependence of  $\epsilon_{33}$  on the frequency. New works by Kleemann et al. [46] show that  $\epsilon_{33}$  (10<sup>-4</sup> Hz) at  $T = 60$  °C is larger by a factor of 2 compared to  $\epsilon_{33}$  (10<sup>2</sup> Hz). This is in very good agreement with our results: If we re-evaluate our data for  $T = 60$  °C with the new value of  $\epsilon_{33}$ , we obtain  $N_{\text{eff}} = 1.81 \times 10^{23} \text{ m}^{-3}$ , which is the value already observed for the low-temperature range. Unfortunately, the very-low frequency values of  $\epsilon_{33}$  are not available for a larger temperature range  $52 \text{ °C} \leq T \leq 65 \text{ °C}$ . The electrooptic coefficient  $r_{33}$  continues to increase in this phase, driven by the steady increase of  $\epsilon_{33}$  with the temperature.

When a temperature of 65 °C is exceeded, the effective determination of  $N_{\text{eff}}$  becomes very difficult. The parameter  $B$  in Eq. (6), which is used to determine  $N_{\text{eff}}$ , is very sensitive on the angular distribution of  $\Gamma(\theta)$ . At higher temperatures,  $\Gamma(\theta)$  becomes rather flat and featureless, making it difficult to obtain a good fitting value of  $B$ . However, the electrooptic coefficient  $r_{33}$  can still be determined, since the parameter  $A$  in Eq. (6), which is used in the determination of  $r_{33}$ , depends mainly on the amplitude of the scattered light, not so much on its angular distribution. We observe that  $r_{33}$  decreases strongly for  $T \geq 65$  °C, corresponding to the decrease of  $\epsilon_{33}$  and  $P_s$  in this temperature range (comp. Eq. (4)). It means that SBN enters the deep relaxor phase where the polar regions of

nm- and  $\mu\text{m}$ -scale (polar clusters) become practically independent, local  $P_s$  vectors are disordered and the electric polarization in neighbouring clusters is mutually compensated. As a result, the value of  $r_{33}$  averaged through the whole volume of the crystal differs from the local values. Thus, in the experiment we measure the decrease of the macroscopic value of the electrooptic coefficient.

For temperatures of 100 °C and above, the scattering pattern becomes symmetrical, indicating that there is no more gain coefficient  $\Gamma(\theta)$  above this temperature, corresponding to a vanishing electrooptic coefficient and a final transition into a centrosymmetric phase.

## 5. Summary

The light-induced polarization–isotropic scattering in SBN61:Ce (0.66 mol%) has been studied in detail for a temperature range including the phase transition temperature. The temperature evolution of the scattering pattern has been examined with respect to changes of the optical parameters of the crystal at the phase-transition from the ferroelectric to the paraelectric phase. Both the electrooptic coefficient  $r_{33}$  and the effective trap density  $N_{\text{eff}}$  could be deduced from the angular distribution of the scattered intensity. This allows us to obtain these important physical parameters from one simple measurement setup without many requirements to mechanical or optical stability and without the need to influence the domain structure with external electric fields.

## Acknowledgements

This work was supported by the DFG (project SPP 1056/WO 618/3-3 and project TFB13/A3) and INTAS (Project 01-0173). M. Goulkov gratefully acknowledges support from the DFG for his stay in the Institut für Mineralogie at the Universität zu Köln. Authors thank the referee for wholesome comments which have enabled us to improve the quality of this paper.

## References

- [1] H.Y. Zhang, X.H. He, Y.H. Shih, S.H. Tang, *Opt. Commun.* 86 (1991) 509.
- [2] F. Micheron, G. Bismuth, *Appl. Phys. Lett.* 20 (1972) 79.
- [3] Y. Quiao, S. Orlov, D. Psaltis, R.R. Neurgaonkar, *Opt. Lett.* 18 (1993) 1004.
- [4] L. Zhang, Z. Shao, X. Mu, H. Chen, M. Jiang, *Opt. Commun.* 123 (1996) 587.
- [5] S. Ducharme, J. Feinberg, R.R. Neurgaonkar, *IEEE J. Quantum Electron.* QE-23 (1987) 2116.
- [6] A.A. Ballmann, S.K. Kurtz, H. Brown, *J. Cryst. Growth* 10 (1971) 185.
- [7] K. Megumi, H. Kozuka, M. Kobayashi, Y. Furuhatu, *Appl. Phys. Lett.* 30 (1977) 631.
- [8] B. Jimenez, C. Alemany, J. Mendiola, E. Maurer, *Ferroelectrics* 38 (1981) 841.
- [9] P.G.R. Smith, R.W. Eason, *Appl. Phys. Lett.* 69 (1996) 1509.
- [10] A.S. Kewitsch, T.W. Towe, G.J. Salamo, A. Yariv, M. Zhang, M. Segev, E.J. Sharp, R.R. Neurgaonkar, *Appl. Phys. Lett.* 66 (1995) 1865.
- [11] Y.Y. Zhu, J.S. Fu, R.F. Xiao, G.K.L. Wong, *Appl. Phys. Lett.* 70 (1997) 1793.
- [12] G.A. Smolenskij, V.A. Isupov, A.I. Agranovskaya, S.N. Popov, *Sov. Phys. Solid State* 2 (1961) 2584.
- [13] T. Granzow, U. Dörfler, Th. Woike, M. Wöhlecke, R. Pankrath, M. Imlau, W. Kleemann, *Appl. Phys. Lett.* 80 (2002) 470.
- [14] R.A. Rupp, J. Seglins, U. van Olfen, *Phys. Stat. Sol. (b)* 168 (1991) 445.
- [15] T. Kume, K. Nonaka, M. Yamamoto, S. Yagi, *Appl. Opt.* 37 (1998) 334.
- [16] B. Fischer, M. Cronin-Golomb, J.O. White, A. Yariv, R.R. Neurgaonkar, *Appl. Phys. Lett.* 40 (1982) 863.
- [17] M. Aillerie, N. Théofanous, M.D. Fontana, *Appl. Phys. B* 70 (2000) 317.
- [18] U.B. Dörfler, R. Piechatzek, Th. Woike, M.K. Imlau, V. Wirth, L. Bohatý, T. Volk, R. Pankrath, M. Wöhlecke, *Appl. Phys. B* 68 (1999) 843.
- [19] V.V. Voronov, I.R. Dorosh, Yu.S. Kuz'minov, N.V. Tkachenko, *Sov. J. Quantum Electron.* 10 (1980) 1346.
- [20] V.V. Obuhovski, A.V. Stoyanov, *Sov. J. Quantum Electron.* 12 (1985) 563.
- [21] N.V. Kukhtarev, V.P. Markov, S.G. Odoulov, M.S. Soskin, V.L. Vinetskii, *Ferroelectrics* 22 (1979) 961.
- [22] K. Buse, U. van Stevendaal, R. Pankrath, E. Krätzig, *J. Opt. Soc. Am. B* 13 (1996) 1461.
- [23] J. Feinberg, *J. Opt. Soc. Am.* 72 (1982) 46–51.
- [24] A.A. Zozulya, M. Saffman, D.Z. Anderson, *Phys. Rev. Lett.* 73 (1994) 818.
- [25] M. Goulkov, M. Imlau, R. Pankrath, T. Granzow, U. Dörfler, Th. Woike, *J. Opt. Soc. Am. B* 20 (2003) 307.
- [26] T. Granzow, U. Dörfler, Th. Woike, M. Imlau, R. Pankrath, M. Wöhlecke, W. Kleemann, *Phys. Rev. B* 63 (2001) 17401.
- [27] M.D. Ewbank, R.R. Neurgaonkar, W.K. Cory, J. Feinberg, *J. Appl. Phys.* 62 (1987) 374.
- [28] P. Solymar, D.J. Webb, A. Grunnet-Jepsen, *The Physics and Applications of Photorefractive Materials*, Clarendon Press, Oxford, 1996.
- [29] P. Yeh, *Introduction to Photorefractive Nonlinear Optics*, John Wiley and Sons, New York, 1993.
- [30] Th. Woike, G. Weckwerth, H. Palme, R. Pankrath, *Solid State Commun.* 102 (1997) 743.
- [31] B.I. Sturman, F. Agullo-Lopez, M. Carrascosa, L. Soly-mar, *Appl. Phys. B* 68 (1999) 1013.
- [32] A.M. Prokhorov, Yu.S. Kuz'minov, *Ferroelectric Crystals for Laser Radiation Control*, Adam Hilger, Bristol, 1990.
- [33] J.R. Oliver, R.R. Neurgaonkar, L.E. Cross, *J. Appl. Phys.* 64 (1988) 37.
- [34] R.A. Vazquez, F.R. Vachss, R.R. Neurgaonkar, M.D. Ewbank, *J. Opt. Soc. Am. B* 8 (1991) 1932.
- [35] R. Grousson, S. Mallick, S. Odoulov, *Opt. Commun.* 51 (1984) 342.
- [36] B.I. Sturman, *Sov. Phys. JETP* 73 (1991) 593.
- [37] M.Yu. Goulkov, S.G. Odoulov, B.I. Sturman, *Appl. Phys. B* 56 (1993) 223.
- [38] M.Yu. Goulkov, T. Granzow, U. Doerfler, Th. Woike, M. Imlau, R. Pankrath, *Appl. Phys. B*, to be published.
- [39] B. Sturman, S. Odoulov, M. Goulkov, *Phys. Rep.* 276 (1996) 197.
- [40] Th. Woike, T. Granzow, U. Dörfler, Ch. Poetsch, M. Wöhlecke, R. Pankrath, *Phys. Stat. Sol. (a)* 186 (2001) R13.
- [41] J. Dec, W. Kleemann, Th. Woike, R. Pankrath, *Eur. Phys. J. B* 14 (2000) 627.
- [42] L.E. Cross, *Ferroelectrics* 76 (1987) 241.
- [43] A.S. Bhalla, R. Guo, L.E. Cross, G. Burns, F.H. Dacol, R.R. Neurgaonkar, *Phys. Rev. B* 36 (1987) 2030.
- [44] V. Wirth, *Temperaturabhängige elektrooptische und elektrostriktive Untersuchungen an Kristallen mit ferroischen Phasenumwandlungen*, Dissertation, Köln, 1999.
- [45] K. Onuki, N. Uchida, T. Saku, *J. Opt. Soc. Am.* 62 (1972) 1030.
- [46] W. Kleemann, J. Dec, S. Miga, Th. Woike, R. Pankrath, *Phys. Rev. B* 65 (2002) 220101.